*J Mater Sci* (2025) 60:3430–3453

Metals & corrosion

# On the martensitic phase transformation and grain boundary character evolution in laser powder bed fusion 17-4 precipitation hardened stainless steel

Michael P. Haines[1], Ehsan Farabi[1], Nima Haghdadi[1], and Sophie Primig[1,*]

[1] *School of Material Science and Engineering, UNSW Sydney, Sydney, NSW 2052, Australia*

**Received:** 25 October 2024
**Accepted:** 11 January 2025
**Published online:**
28 January 2025



## ABSTRACT

Laser powder bed fusion (L-PBF) of 17-4 precipitate hardened (PH) stainless steel is well-known for its significant variations in reported microstructures. While recent research has provided better understanding of the phase transformation pathways leading to as-built microstructures of $\delta$-ferrite, martensite, and/or austenite, reproducible and fully martensitic microstructures would be more desirable to provide strength and age-hardening potential. However, the understanding of the martensitic phase transformation as a function of 17-4 PH powder feedstock and L-PBF route remains limited. We aim to fill this gap by comparing builds from two processing routes with different powder feedstocks and processing parameters. As-built and heat treated (1 h at 1040 °C followed by water quenching) conditions are considered. We reveal the link between the parent austenite grain size (PAGS) and the resulting martensite microstructure. A detailed five-parameter characterization of interfaces shows that a smaller PAGS results in improved grain boundary connectivity and higher length fractions of 60°/[1 1 $\bar{1}$] and 10.5°/[0 1 1] intervariant boundaries in the martensite. Computational material science demonstrates the link between the processing parameters and composition with microstructural variations and development. Our results are broadly applicable to steel L-PBF, underpinning that refinement of martensite will improve the grain boundary network and selection of desirable intervariants. This is expected to impact material properties such as toughness, strength, intergranular corrosion, cracking, slip, and the segregation of impurities.

Handling Editor: Megumi Kawasaki.

Address correspondence to E-mail: s.primig@unsw.edu.au

Springer

https://doi.org/10.1007/s10853-025-10645-8

## GRAPHICAL ABSTRACT

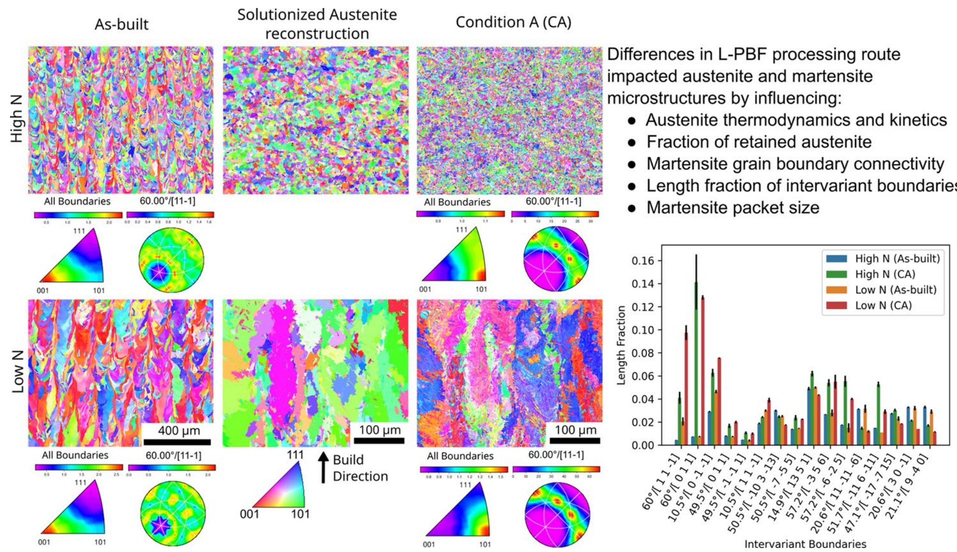


## Introduction

Metal additive manufacturing (AM), while often advertised for being able to easily make highly complex geometrical features, still suffers from significant uncertainties in microstructure and property control [1–3]. There are numerous current efforts toward understanding these microstructural variations and even developing the ability for site-specific microstructural control [1, 4–8]. For laser powder bed fusion (L-PBF), 17-4 precipitation hardened (PH) stainless steel has been a material of interest due to its attractive property profile including high strength and toughness combined with excellent corrosion resistance. 17-4 PH has numerous applications involving complex parts in aerospace, marine environments, power generation, and the chemical industries [9–13]. However, there have been challenges in obtaining consistent microstructures using 17-4 PH in L-PBF due to the sensitivity of its phase transformations to the chemical composition and processing parameters.

17-4 PH has been designed to carefully balance the fraction of retained austenite and martensite while avoiding the formation of unfavorable $\delta$-ferrite following traditional cast and wrought processing routes [14]. The desired 17-4 PH microstructural evolution during processing is first, the solidification as $\delta$-ferrite, followed by a diffusional transformation to austenite, and then a displacive transformation to martensite. However, due to both compositional variations permitted by the material specification and sensitivity to cooling rates inherent to the L-PBF process, 17-4 PH sees large variations in final as-built and heat treated microstructures [15–20]. It has been well established that powder composition plays a large role in influencing the microstructures in the as-built condition due to the potential variation in N content [17, 21, 22]. Works have shown that lower N content powder is more likely to form $\delta$-ferrite and minimal amounts of austenite in the as-built, while an increase in N makes the formation of austenite more likely. In certain cases, where the composition favors faster austenite kinetics but where the martensite start temperature is not significantly suppressed, even the formation of martensite has been reported [16, 23]. Other publications have demonstrated the impact of processing parameters on the formation of austenite, with lower cooling rates resulting in a greater amount of austenite formation [3, 18].

In the consideration of different heat treatments, many publications have shown the formation of a predominantly martensitic microstructure with a limited fraction of retained austenite [17, 19, 22–26]. It should be noted, however, that these works mostly consider the difference in powder composition with minimal detailed analysis on the resulting

**Table 1** Composition (wt.%) of 17-4 PH stainless steel powder measured from inductively coupled plasma atomic emission spectrometry (ICP-AES)

| | Fe | Cr | Ni | Cu | Mn | Si | Nb | Mo | N | C | $Cr_{eq}/Ni_{eq}$ |
|---|---|---|---|---|---|---|---|---|---|---|---|
| *High N* | | | | | | | | | | | |
| Powder | Bal | 16.1 | 4.34 | 3.81 | 0.87 | 0.71 | 0.32 | 0.13 | 0.10 | 0.03 | 1.96 |
| Build | Bal | 16.8 | 4.57 | 3.92 | 0.90 | 0.92 | 0.37 | 0.12 | 0.09 | 0.02 | 2.04 |
| *Low N* | | | | | | | | | | | |
| Powder | Bal | 16.5 | 4.01 | 3.88 | 0.64 | 0.57 | 0.34 | 0.08 | 0.02 | 0.02 | 2.78 |
| Build | Bal | 16.0 | 3.94 | 3.61 | 0.56 | 0.60 | 0.25 | 0.07 | 0.077 | 0.01 | 2.33 |

martensitic microstructure. Yet, multiple properties of the martensitic microstructure, including the character of the martensitic interfaces and martensite packet size impact the toughness [27], strength [28], intergranular corrosion [29–31], cracking [32], slip [33], and segregation of impurities within stainless steels.

Overall, the parent austenite grain structure and size play a significant role in the transformation to martensite during quenching [34–37]. The austenite grain boundaries more often serve as the nucleation sites for martensite. For any given austenite grain, 24 crystallographically equivalent orientated martensite variants/orientations can be formed according to the Kurdjumov–Sachs (K–S) orientation relationship (Table S1 in the supplementary materials) [38, 39]. The impingement of these variants hypothetically leads to 23 lattice misorientations, which can be reduced to 16 distinct intervariant boundaries due to crystal symmetry. The parent austenite grain size (PAGS) determines the packet size and intervariant selection of the martensite grains and alters the driving force for martensite transformation by influencing the strain acting against it. However, compositional variations can alter lattice parameters and lattice strains associated with the austenite to martensite transformation, resulting in unique grain boundary networks [35, 40].

The martensitic transformation and its relationship to processing parameters and powder composition in L-PBF 17-4 PH have received little attention in the literature, despite extensive analyses in traditionally manufactured materials, leaving a significant gap in the understanding of the phase transformation characteristics and martensite microstructure development in AM materials. The current study aims to reveal the complexities in the martensitic transformation in L-PBF 17-4 PH through advanced characterization of the martensite hierarchy. Two sets of builds are considered in this study following two different processing routes. Both builds underwent solution heat treatment and quenching (CA heat treatment) to obtain martensitic microstructures. The results demonstrate that vastly different martensitic microstructures are formed, with significant differences in microstructure refinement. Through an in-depth analysis of the as-built and heat treated microstructures, the differences are linked back to differences in the powder composition and processing parameters. This is complemented by a comprehensive analysis of interfaces including intervariant boundary populations, their habit planes, and their connectivity. Overall, the advanced understanding of the martensitic transformation in 17-4 PH, within the context of AM, will help to reduce microstructural variations, enable microstructure refinement, and, in turn, AM of 17-4 PH builds with superior properties.

# Materials and methods

## Experimental procedures

Two different builds were produced utilizing two different gas atomized 17-4 PH powders supplied by 3D Systems and General Electric (GE), respectively. The 3D systems powder was used in a 3D Systems ProX 300 and the GE powder was used in a GE Concept Laser MLab 200R, respectively. Both powder compositions are given in Table 1. The $Cr_{eq}/Ni_{eq}$ ratio [22], often used as a guide toward the preference for $\delta$-ferrite versus austenite formation, is also given in Table 1. The major distinguishing attribute between the two powders is their N content. The 3D systems powder was gas atomized under $N_2$. The GE powder was gas atomized under Ar. From henceforth, builds printed using the 3D system's powder will be referred to as the 'High N' builds, and the builds utilizing the GE powder will be referred to as the 'Low N' builds.

All builds were printed with $10 \times 10 \times 15$ mm$^3$ cuboidal geometries. Schematics of the geometry

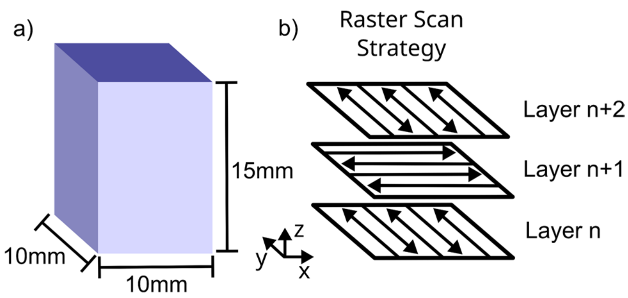


**Figure 1** **a** Schematic with dimensions of the cuboidal geometries printed. **b** Schematic of the raster geometry with the 90° rotation per layer

**Table 2** Processing parameters used in for printing the Low N and High N builds

| | Low N | High N |
|---|---|---|
| Machine | GE Concept Laser MLab 200R | 3D Systems ProX 300 |
| Laser power (W) | 180 | 127.5 |
| Laser velocity (mm/s) | 1170 | 1200 |
| Laser diameter (μm) | 75 | 90 |
| Hatch spacing (μm) | 82 | 50 |
| Layer height (μm) | 30 | 40 |

with reference coordinates are given in Fig. 1a. The compositions of the builds are presented in Table 1. The High N build showed a slight decrease in the N content compared to the initial powder, while the low N samples saw an increase in N content. Of note, the Low N build still shows a higher $Cr_{eq}/Ni_{eq}$ compared to the High N builds. The processing parameters for the High N and Low N builds are given in Table 2 and are the standard machine parameters recommended by the manufacturers. The energy density given as $E_d = P/vlh$ was $5.9 \times 10^{14}$ J and $6.25 \times 10^{14}$ J for the High N and Low N builds, respectively, with $P$ being the laser power, $v$ the laser velocity, $l$ the layer height, and $h$ the hatch spacing. Both builds utilized a raster scan strategy with a 90° rotation. Schematics of the scan strategy are given in Fig. 1b. The High N builds were built in an $N_2$ atmosphere with a minimum purity of 99.8%, while the Low N builds were built in an Ar atmosphere with a purity of 99.9970%. Selected samples went through the standard CA heat treatment step, based on ASTM standard A705/A705M-23 [41], to encourage martensitic transformation which entailed heat treating the sample at 1040 °C for 1 h followed by water quenching [42, 43]. Overall, the process of utilizing two different machines with powders from two different manufacturers followed by a standard heat treatment regime mimics a potential real-world scenario, where two manufactures are tasked with the printing of specific geometries for a particular part. The square geometries were chosen here for simplicity while still representing potential changes in microstructure due to process variations.

Metallographic sample preparation involved grinding using SiC papers up to 4000 grit. Polishing was done to a mirror finish down to 1 μm diamond suspensions. Samples were then electro-polished using Struers A2 etchant at 25 V for 20 s. To reveal melt pool boundaries, Fry's reagent (40 mL HCl, 5 g $CuCl_2$, 30 mL water, and 25 mL ethanol) was utilized for 5 s. Electron backscatter diffraction (EBSD) was conducted using a Hikari-EDAX camera mounted on a JEOL 7001F scanning electron microscope (SEM). EBSD data were captured using a 13 nA probe current, 20 kV acceleration voltage and 8 × 8 binning. A step size of 0.5 μm for as-built samples and 0.2 μm for CA samples was utilized. EBSD data analysis was performed using the TSL software. Prior austenite grain reconstruction was done via TSL utilizing a probabilistic back construction technique outlined by Ranger et al. [44]. The EBSD data were cleaned first through a dilation clean-up with a minimum grain size limit of 5 pixels to remove unindexed points. A single average orientation was then assigned to each grain by considering the orientations of neighboring pixels with a tolerance of 5°. Lastly, during the grain boundary reconstruction, the boundaries were smoothed considering a deviation of 2 pixels. The extracted boundaries were then used for calculating the five-parameter character distribution of interfaces using the approach developed by Rohrer et al. [45]. For X-ray diffraction (XRD), the samples underwent the same grinding and electropolishing routine as for EBSD. The lattice parameters of the CA samples were determined using a Panalytical X'pert PRO MRD XL machine. The XRD scans were conducted with a Cu source, running at an applied voltage of 50 kV and a current of 40 mA. The lattice parameters for martensite and austenite if present in the XRD within the High N and Low N samples were determined through Bragg's law.

Table 3 Properties used in the analytical heat transfer simulation

| Property | Low N | High N | References |
|---|---|---|---|
| $T_0$(K) | 348.15 | | |
| $T_l$(K) | 1659 | | |
| $k$(W m$^{-1}$ K$^{-1}$) | 22.6 | | [51] |
| $c_p$(J Kg$^{-1}$ K$^{-1}$) | 460.0 | | [51] |
| $\rho$(Kg m$^{-3}$) | 7800.0 | | [51] |
| $\eta$ | 0.8 | 1.1 | |
| $\sigma_z$(μm) | 70 | 80 | |

## Thermal modeling

Thermal simulations are applied to better understand resulting differences in microstructural evolution between the High N and Low N builds due to differences in processing conditions, and simulations will be used to underpin the discussion of the experimental results in the following. One could consider all phenomenological contributions such as fluid flow, latent heat, evaporation, and convective heat losses [46]. However, the consideration of broader melt pool trends is seen to be sufficient here. Therefore, a simple conduction only analytical heat transfer model was utilized that was developed by Oak Ridge National Laboratory [47]. This code has been validated in multiple studies for modeling the thermal conditions within the AM process [5, 6, 48, 49] and models the heat transfer conditions over an entire layer. The underlying model is based on an analytical solution for a moving volumetric Gaussian heat source proposed by Nguyen et al. [50]:

$$T - T_0 = \frac{2\eta Q}{\rho c\left(\frac{\pi}{3}\right)^{3/2}} \int_0^t \frac{1}{\sqrt{\phi_x \phi_y \phi_z}} \times \exp\left(\frac{-3x(t')^2}{\phi_x} - \frac{3y(t')^2}{\phi_y} - \frac{3z(t')^2}{\phi_z}\right) dt'$$

where $T_0$ is the initial preheat temperature, $T$ is the temperature, $Q$ is the beam power, $\eta$ is the laser absorption coefficient, $\rho$ is the density, $t$ is time, $c$ is the specific heat, and $\phi_i = 12\alpha(t - t\prime) + \sigma_i^2$ for $i = x, y, z$. Thermal diffusivity $\alpha = k/\rho c$ where $k$ is the thermal conduction. The width of the volumetric heat source is described by $\sigma_x$, $\sigma_y$, and $\sigma_z$. More details related to the theory behind these analytical codes can be found elsewhere [47]. The material parameters used for both builds are given in Table 3. The liquidus temperature ($T_l$) used for tracking the melt pool was obtained from ThermoCalc. All other properties were either calibrated from melt pool geometry or obtained from references where relevant.

# Results

## Microstructure evolution

The inverse pole figure maps (IPF), phase maps, and pole figures from EBSD for the as-built builds, parallel to the build direction, are presented in Fig. 2. Both builds show more randomly oriented crescent shaped grains sandwiched between thin long grains oriented in the < 100 > direction parallel to the build direction. The grain structure between the two builds is clearly influenced by the differences in processing parameters and the distance between the crescent grain structures decreased for the High N build compared to the Low N build. Overall, the High N build has smaller grains with a calculated average grain diameter of ~ 22 μm compared to ~ 65 μm for the Low N build. The High N build also shows a greater degree of randomness in texture with an intensity of 2.35 oriented roughly in the < 100 > parallel to the build direction. The Low N build has an intensity of 4.21 oriented similarly in the < 100 > parallel to the build direction. The lack of a lath microstructure in either IPF map indicates that both builds have solidified with a $\delta$-ferrite microstructure and that martensite is not present. The phase maps show that both builds contain mostly a body centered cubic (BCC) $\delta$-ferrite microstructure with a higher content of grain boundary face-centered cubic (FCC) austenite occurring in the High N build, due to the lower $Cr_{eq}/Ni_{eq}$ ratio. Further analysis of the FCC pole figures separately (Fig. S1 in the supplementary) indicates a preference for the FCC to be oriented in the < 110 > direction. Such preferential grain direction, with a lack of grains orientated in the < 100 > direction parallel to the build direction, indicates a solid–solid transformation occurred from $\delta$-ferrite to austenite. The proceeding analysis of grain boundaries will, however, give further proof for the formation of $\delta$ -ferrite without the need to rely on more complex

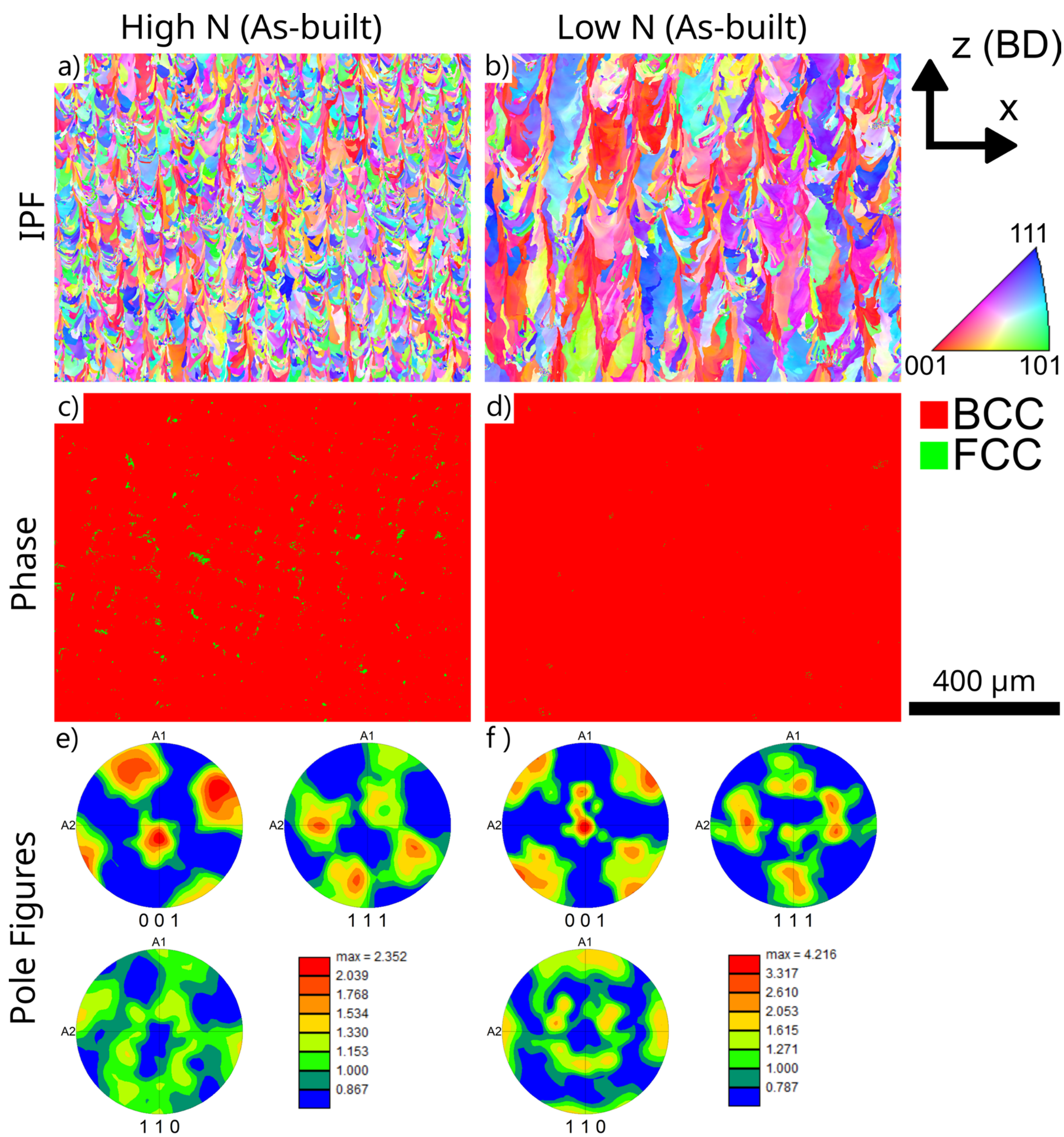


**Figure 2** EBSD data of the as-built **a**, **c** High N and **b**, **d** Low N builds in the XZ plane. **a**, **b** show IPF maps, **c**, **d** phase maps, and **e**, **f** the pole figures, respectively.

methods such as neutron diffraction for a distinction between ferrite and martensite.

IPF maps, phase maps, and IPF austenite reconstructions for the CA heat treated builds are given in Fig. 3, while a separation of the BCC and FCC phases for Fig. 2c are given as Fig. S2 in the supplementary materials. IPF maps show that for both builds, a significantly refined microstructure has formed when compared to the as-built counterparts. The prior solidified $\delta$-ferrite microstructure has been replaced by a mostly martensitic microstructure due to the CA heat treatment that is evident by the lack of any AM solidification structure and, in the case of the Low N builds, lath microstructure. Significant differences in the refinement of the microstructure can be seen between the High N and Low N builds with the High N build having a smaller lath/packet size compared to the Low N build. These phase maps further reveal a stark difference in the fraction of retained austenite with the High N build showing a

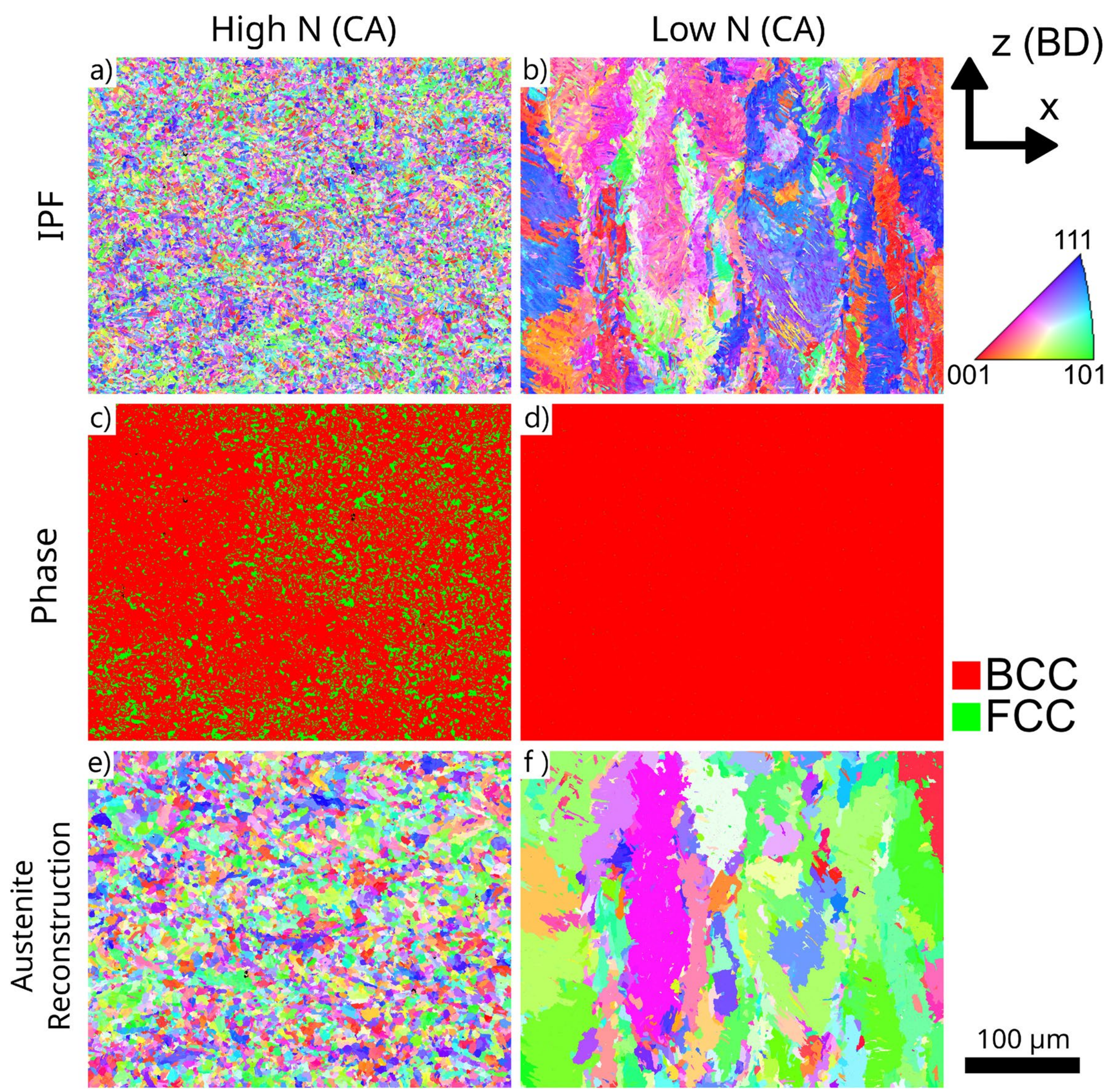


**Figure 3** EBSD maps of the builds in CA condition. **a**, **c** High N and **b**, **d** Low N builds in the XZ plane where **a**, **b** show IPF maps, **c**, **d** phase maps, and **e**, **f** the austenite reconstruction.

high fraction of retained austenite (~ 9.7%), while the Low N builds only detected an insignificant number of points from EBSD (~ 0%) (Fig. 3c, d). The IPF maps of the reconstructed austenite show that the High N build has notably smaller and more equiaxed parent austenite grains compared to the Low N build with PAGS being ~ 10.2 ± 0.4 µm and ~ 52.6 ± 0.1 µm for the High N and Low N builds, respectively. The difference in reconstructed PAGS indicates that the processing parameters and composition of the powder likely plays a role in influencing the nucleation and growth of austenite and the proceeding transformation to martensite.

XRD results for the CA builds are provided in Fig. 4. The results show that no austenite was detected in the Low N build, while austenite was detected in the High N build. Only the BCC/martensite matrix phase and FCC/austenite phases could be detected. While oxides and carbides often form within L-PBF steel builds, these are usually too small to be detected through laboratory-based XRD.

## Misorientation angle distributions

An analysis of the BCC–BCC grain boundary misorientation angle distributions (Fig. 5) reveals a

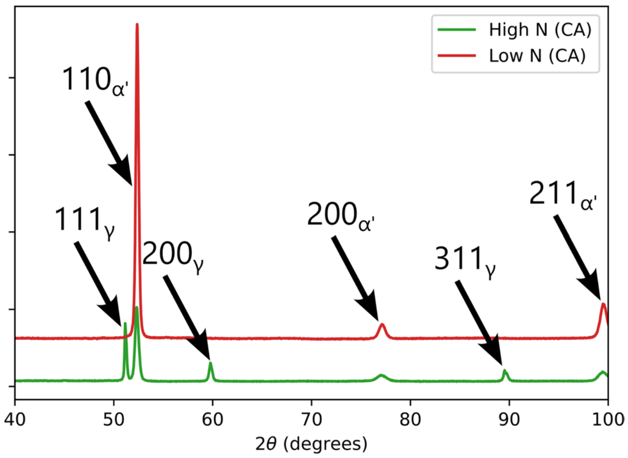


**Figure 4** XRD results for the Low N CA and High N CA builds revealing an absence of austenite in Low N.

significant difference between the as-built and CA builds, with smaller differences between High N and Low N builds. The as-built builds show relatively random misorientation angle distributions. While an indication for being predominantly $\delta$-ferrite was established through the as-built grain structure, the relatively random distribution in the misorientation angle distribution underpins $\delta$-ferrite formation further. Martensite is expected to have the majority of its misorientations correlate to K–S intervariant boundaries as will be seen in the CA heat treated builds [39, 52]. It should be noted that martensite can also follow an N–W OR, and, as a result, these martensite boundaries will not only include K–S intervariant boundaries, but also possibly N–W intervariant boundaries, and mixed boundaries [53]. A full analysis of all these intervariant boundaries would be a major task and, therefore, we have chosen to focus on the K–S intervariant boundaries here as they are the majority of boundaries present. Between the two builds, the Low N build shows a marginally higher distribution of misorientation angles toward lower values (< 20°). The CA builds from both builds show considerable peaks around 60° and smaller peaks at 10–15°, which is expected as these angles fall within intervariant boundaries resulted from a K–S orientation relationship (Table S1 in the supplementary materials) [39, 52]. Compared to the High N build, the Low N build has a much higher peak

**Figure 5** BCC/BCC misorientation angle distributions for **a** as-built High N and Low N builds and **b** CA High N and Low N builds.

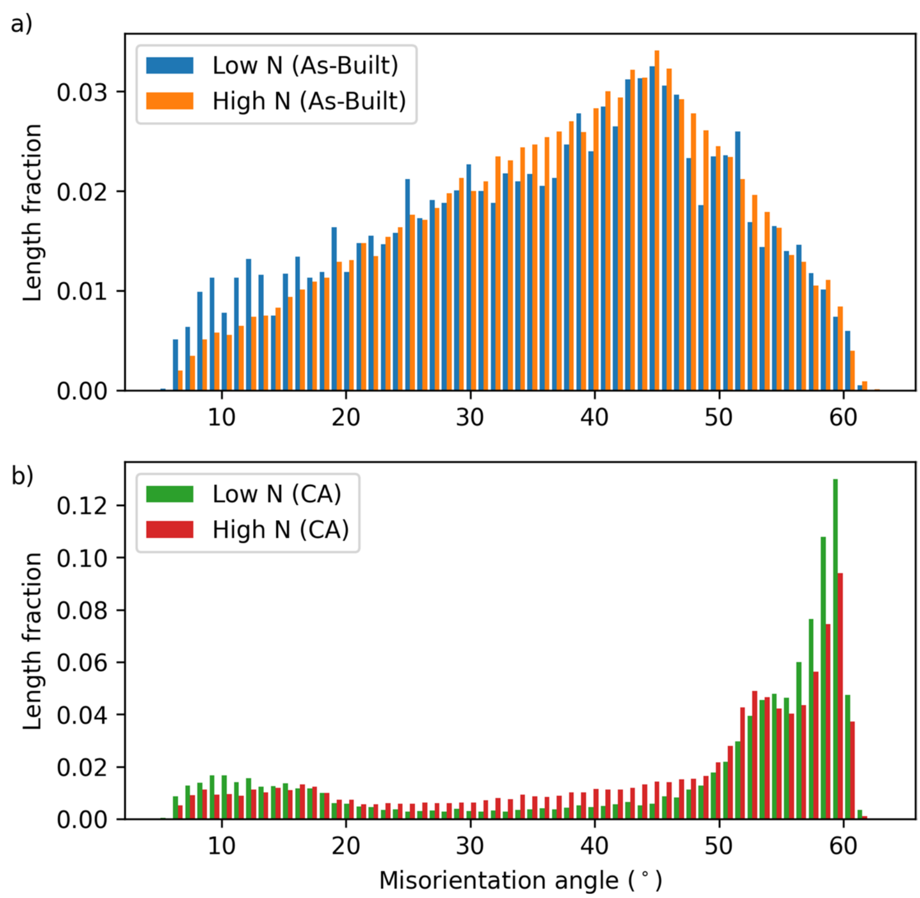

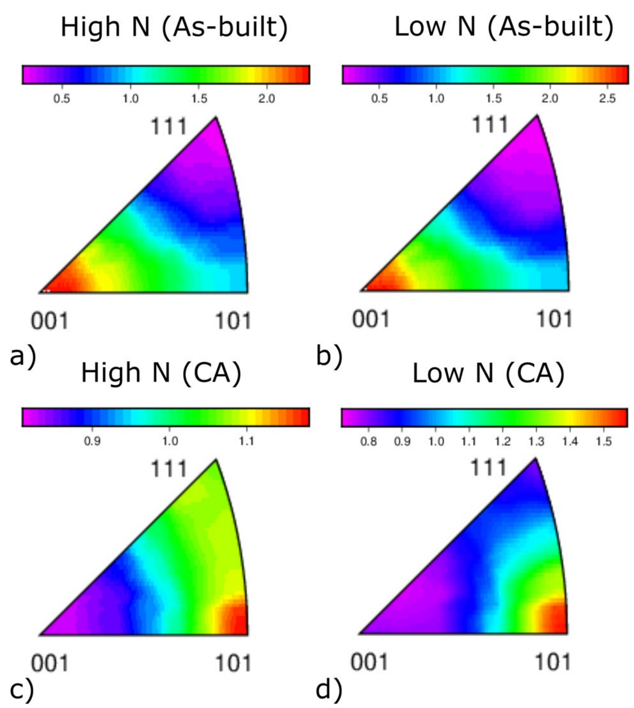


**Figure 6** Distributions of grain boundary planes in **a**, **b** High N and Low N as-built (ferritic) and **c**, **d** CA (martensitic) samples.

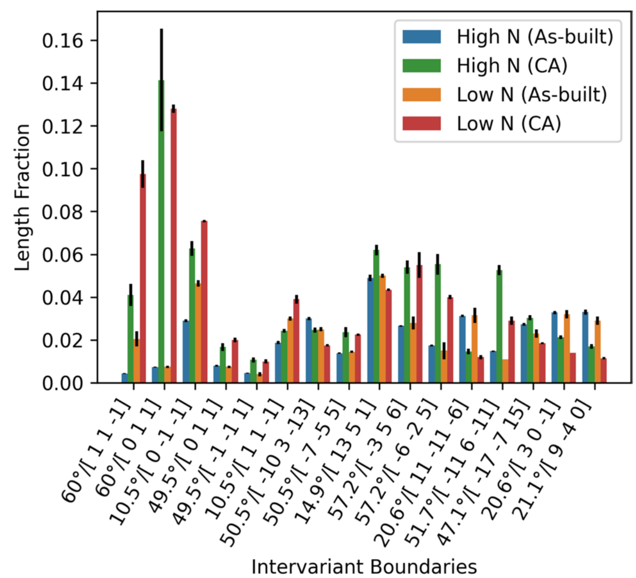


**Figure 7** Distribution of intervariant boundaries associated with the K–S orientation relationship for the BCC phase (ferrite and martensite) in the as-built and CA conditions of the High N and Low N builds.

around 60° and a greater number of misorientation angles ~ 10°. The High N build, however, has a slightly greater number of misorientation angles around 22–46° which correlate to the impingement of variants from either side of a given parent austenite grain boundary [54].

## Grain boundary plane distributions

The grain boundary plane distribution for each build irrespective of the misorientation angle is given in Fig. 6. The as-built conditions show maximum multiples of a random distribution (MRDs) of ~ 2.3 and ~ 2.7 at the (100) plane with minima of ~ 0.2 and ~ 0.2 along the (111) plane for the High N and Low N builds, respectively. The CA builds on the other hand show maximum MRDs of ~ 1.2 and ~ 1.6 at the (101) plane with minima of ~ 0.8 and ~ 0.7 along the (100) plane for the High N (CA) and Low N (CA) builds, respectively. Only minor differences in distributions were noted between the two CA builds with small differences in populations of the (111) planes.

## Intervariant boundary character distributions

For all builds, the distributions of intervariant boundaries expected from a transformation following a K–S orientation relationship (refer to supplementary Table S1) are given in Fig. 7. Overall, the distribution of the intervariant boundaries varies depending on whether the build is in the as-built or CA condition. The as-built builds do not show any strong K–S orientation relationship preference. This is expected as these builds has not experienced any solid-state phase transformations. The CA builds, however, show dominant populations of 60°/[0 1 1], 60°/[1 1 $\bar{1}$], 10.5°/[0 1 1], 57.2°/[$\bar{3}$ 5 6] and 51.7/[ $\overline{11}$ 6 $\overline{11}$] intervariants. More specifically, the Low N samples show a greater length fraction of 60°/[1 1 $\bar{1}$] and 10.5°/[0 1 1] intervariant boundaries compared to the High N sample, while the High N sample shows a greater length fraction of 14.9°/[13 5 1] and 51.7[$\overline{11}$ 6 $\overline{11}$] intervariant boundaries compared to the Low N sample.

Figures 8 and 9 present habit plane distributions for most populated K–S intervariant boundaries with misorientation axes of [0 1 1] and [1 1 1], respectively. The theoretical positions of habit planes have also been plotted for the characteristic misorientations using the grain boundary toolbox software by Glowinski [55] and are shown in supplementary Fig. S3. Due to

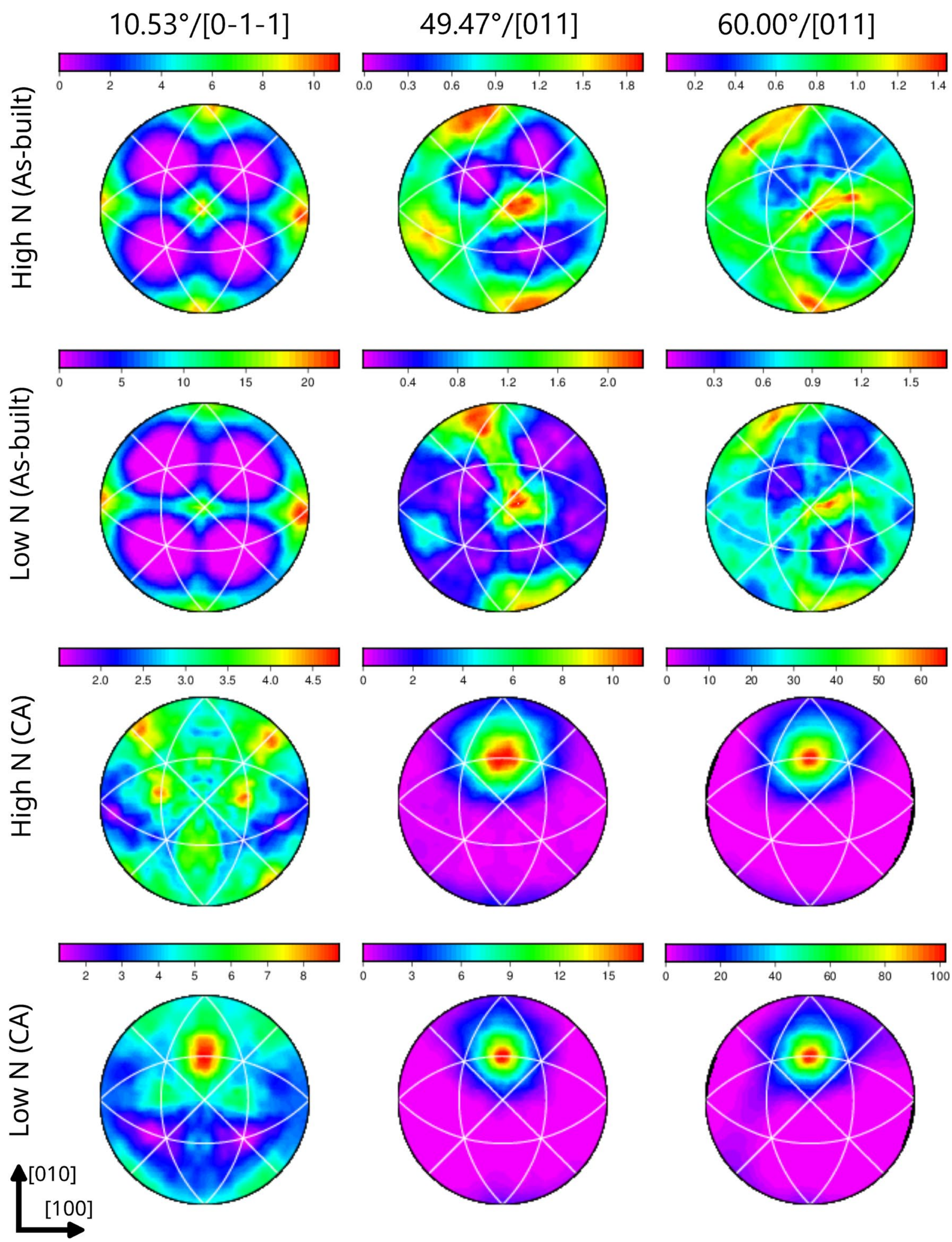


**Figure 8** Distribution of boundary plane normals for boundaries in the as-built **a**–**f** and CA conditions **g**–**l** for High N **a**–**c**, **g**–**i** and Low N **d**–**f**, **j**–**l** at **a**, **d**, **g**, **j** 10.5°/[0–1–1], **b**, **e**, **h**, **k** 49.5°/[011], and **c**, **f**, **i**, **l** 60°/[011].

differences in phase (i.e., $\delta$-ferrite in the as-built builds and martensite in the CA builds), a noticeable difference in the intervariant boundary plane character distribution is observed between the as-built and CA builds. For 10.53° misorientations about the [0 1 1] axis (Fig. 8), maxima are observed for boundaries

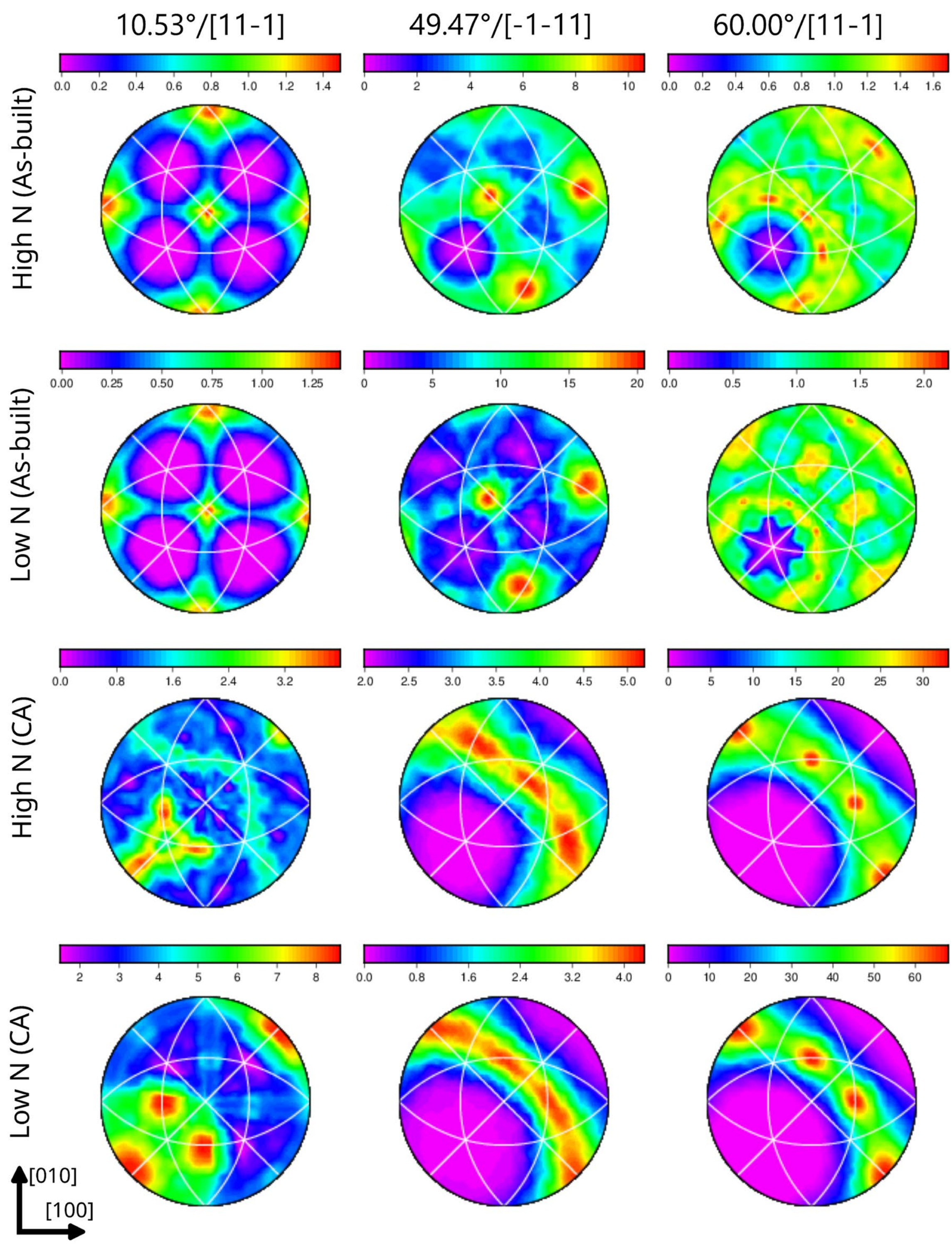


**Figure 9** Distribution of boundary plane normals for boundaries in the as-built **a**–**f** and CA conditions **g**–**l** for High N **a**–**c**, **g**–**i** and Low N **d**–**f**, **j**–**l** at **a**, **d**, **g**, **j** 10.5°/[11–1], **b**, **e**, **h**, **k** 49.5°/[–1–11], and **c**, **f**, **i**, **l** 60°/[11–1].

with twist {1 0 0} orientations for the as-built High N and Low N conditions. Greater differences are noted for the High N and Low N CA conditions. For the High N builds, maxima are seen mostly along tilt and twist boundaries with near {1 0 1} orientations while for Low N builds the peak is seen along a single twist grain boundary with a (0 1 1) orientation. For 49.47° misorientations about the [0 1 1] axis, as-built conditions show similar behavior with maxima along {1 1 4} orientations and with a smaller single peak present at the ($\overline{3}\overline{1}$ 1) orientation. In the CA conditions, both builds show a single peak at the (0 1 1) twist boundary orientation with MRDs of ~ 11 and ~ 17 for the High N and Low N CA conditions, respectively. For 60° misorientations, the as-built conditions have diffuse peaks close to {2 0 5} and {$\overline{1}$ $\overline{5}$ 10} planes. The CA conditions show a pronounced peak at (0 1 1) twist boundaries with an intensity of ~ 65 and ~ 100 MRDs for the High N and Low N CA conditions, respectively.

The distribution of intervariant boundary plane characters about the [1 1 1] misorientation axis (Fig. 9) shows similar trends between the as-built and CA conditions. At a misorientation angle of 10.53°, maxima are seen along multiple {1 0 0} orientations for the as-built condition. Under the CA conditions, maxima were along multiple {1 0 1} orientations; however, the Low N CA builds have MRDs at much higher values of ~ 8 compared to the High N CA builds at maximum MRD of ~ 3.8. At the misorientation angle of 49.47°, the as-built condition shows maxima at twist {1 1 4} orientations. The Low N conditions have a higher MRD of ~ 20 compared to the High N conditions with a maximum MRD of ~ 11. For the CA conditions, peaks vary between the High N and Low N builds. The High N and Low N CA conditions have diffuse peaks along twist boundaries with {3 4 7} orientations. For 60° misorientations, the as-built conditions have peaks around the twist boundaries of the {1 0 2} orientations. The CA conditions saw maxima that are on the zone axis of tilt boundaries of {1 1 0} orientations.

## Discussion

The resulting grain boundary characteristics will be greatly influenced by the solidification conditions and the proceeding solid–solid phase transformations; thus, a discussion of these factors is warranted that looks at the connection between processing parameters and composition in conjunction with the solid–liquid and solid–solid phase transformations. Likewise, numerous factors relating to the as-built solidification-based $\delta$-ferrite microstructure will impact the proceeding austenite nucleation. These factors primarily derive from differences in the resulting solidification microstructure and compositional differences. Reasoning for the differences in as-built and heat treated microstructures is possible through analysis of changes in the resulting processing parameters' impact on the solidification microstructure through consideration of the columnar to equiaxed transition (CET), and analysis of epitaxial grain growth at the melt pool boundaries [56–58]. However, changes in heat treated microstructures can be analyzed through the consideration of computational material thermodynamics and kinetics [59].

### Impact of composition and processing parameters on solidification microstructure

Both the Low N and High N as-built microstructures show a primarily $\delta$-ferrite grain structure. Confirmation of the formation of the $\delta$-ferrite microstructure comes from the grain boundary planes in Fig. 6, which show a favored < 100 > direction that is parallel to the build direction. If a transformation-induced plasticity (TRIP) effect had occurred due to sample preparation, then the as-built condition would have seen a strong < 101 > orientation that aligns to expected K–S orientation relationships, which is not the case here. Further, while some austenite is seen in the High N build, this austenite is believed to have formed via a solid–solid transformation based on the FCC pole figures (Fig. S1 in the supplementary materials) showing a favored < 110 > direction not aligned to the build direction. Overall, the differences in the as-built solidification microstructure can mostly be attributed to differences in processing parameters as argued through computational material science calculations given below.

CET calculations here are performed to consider the impact of composition and processing parameters on the solidification microstructure. The CET utilized the methods outlined by some of the current authors [60]. Thermodynamic data were obtained from ThermoCalc using the TCFE11 database, while the thermal gradients and solidification velocity were obtained from the analytical heat transfer simulation described in Sect. "Thermal modeling" utilizing a raster scan strategy as used for both builds. The nucleation density of equiaxed grains was set to $1 \times 10^{15}$ $m^{-3}$, the highest reasonable potential nucleation density cited in AM literature [8]. The CET results are presented in Fig. 10. The different 17-4 PH compositions have little effect on the CET curves, which is consistent with results from

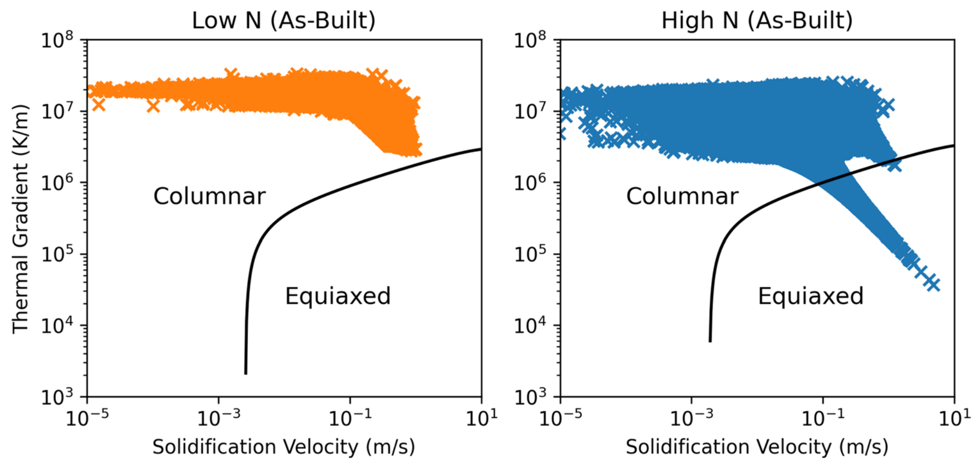


**Figure 10** Columnar to equiaxed transition plots for the **a** Low N and **b** High N as-built conditions overlaid with thermal data from semi-analytical heat transfer simulations.

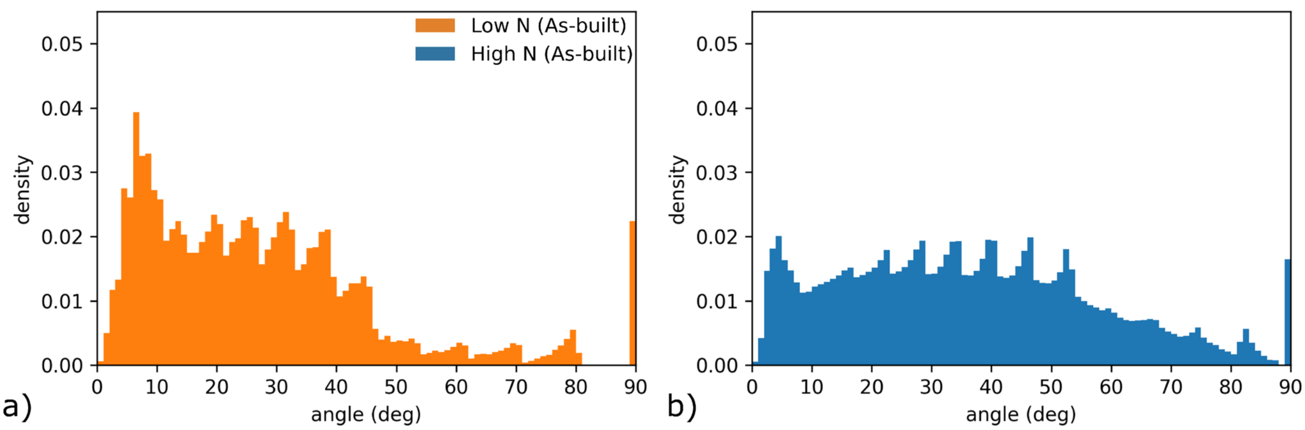


**Figure 11** Comparison of calculated dendritic growth direction for the **a** Low N and **b** High N as-built conditions based on results from the semi-analytical heat transfer simulation.

literature [60] that compositions play a minimal role in impacting the CET. Both processing parameters show a preference toward columnar grain structures. The minority of points that are below the CET curve for the High N build likely occurs at the end of solidification and, thus, are likely to be remelted upon the next layer, limiting any equiaxed grain formation.

The evolution of the grain structure is dependent on multiple factors including the thermal gradient, solidification velocity, and undercooling [61]. The analytical CET model used here only considers the competition between columnar grains and their potential impingement with equiaxed grains that grow ahead of the advancing columnar front [62]. Therefore, there is no consideration, in the CET, on the impact of the melt pool shape on epitaxial grain growth. As grains tend to grow in the direction of the highest thermal gradients, more turbulent melt pool dynamics are likely to encourage numerous different favored grain directions resulting in greater competition [61] and greater epitaxy in the grain structure. The impact of the thermal gradient direction is quantified here using a method proposed by Raghavan et al. [63] by considering the thermal gradients alignment at the solid–liquid interface with respect to the build direction through:

$$\theta = \cos^{-1}\left(G_z / G_{\text{resultant}}\right)$$

where $\theta$ is the angle between the thermal gradient in the build/Z-direction ($G_z$) and the thermal gradient at the solid–liquid interface ($G_{\text{resultant}}$). The output best represents the curvature of the melt pool. Only the bottom 30 µm for the Low N builds and bottom 40 µm for the High N builds were considered here due to the remelting that will occur for any segment of the melt pool above these values. Histograms of the calculated angles are presented in Fig. 11.

Considering the resulting curvature in the melt pool based on the angles presented, the Low N build results in a solid–liquid interface that has thermal gradients distributed more in line with the build direction. The impact is a more consistent preference for grain growth favored in the < 100 > direction parallel to the build direction with consistent growth of fewer grains and less competition (in line with Fig. 2). The High N build, in contrast, has a wider distribution of thermal gradients. Thus, there will be greater competition between grains resulting in the nucleation of grains in different grain directions that do not necessarily align with < 100 > parallel to the build direction [61]. The ultimate outcome is that, due to the processing parameter differences, the High N build has a smaller grain size and greater density of $\delta$-ferrite grain boundaries compared to the Low N builds for the as-built state which will have an impact on the available number of nucleation sites for austenite during the heat treatment step.

## Impact of composition and processing parameters on the transformation of $\delta$-ferrite to austenite

The transformation of the $\delta$-ferrite to austenite will be dictated by both the composition and the solidification microstructures [64–66]. This can be explained first through understanding that the nucleation of the austenite phase will be influenced by the number of nucleation sites, the local diffusion fields around nucleation sites, the driving force for nucleation, and the interfacial energy. Many of these parameters can be estimated through the use of computational thermodynamics and kinetics or through general observations of the microstructure.

Austenite under L-PBF 17-4 PH nucleates at the $\delta$-ferrite grain boundaries [67]. Overall, the high N builds have a higher grain boundary density at 0.154 $\mu m/\mu m^2$ compared to the low N builds at 0.104 $\mu m/\mu m^2$ due to differences in solidification conditions as discussed in the previous section. The higher density of grain boundary results in the High N build having a greater number of nucleation sites for austenite to nucleate from. Further, calculations from ThermoCalc using the TCFE11 database show that the High N builds have a higher driving force for nucleation of austenite compared to the low N builds, increasing from 4.63 to 4.94 J/mol. As such it is expected that the high N builds will see more pronounced nucleation of austenite. The growth of austenite is also expected to be faster in the High N builds due to the differences in composition as the high N builds have a lower $Cr_{eq}/Ni_{eq}$ ratio. In turn, however, due to the greater number of nucleated austenite grains and faster growth rates in the high N builds, the austenite grains quickly impinge on each other resulting in a smaller PAGS. The low N builds comparatively see much slower austenite kinetics. These results have a down the line impact on the martensite block and packet sizes and the resulting martensite intervariant selection as will be discussed in the following.

## The role of composition and processing parameters on austenite to martensite phase transformation and grain boundary network

### *Grain boundary planes in as-built versus CA builds*

The boundary network characteristics play an essential role in the properties of AM builds. For instance, the {110} boundary planes are beneficial for controlling hydrogen embrittlement and dislocation plasticity [28, 68, 69]. Overall, the intervariant boundary plane distributions in the displacively transformed martensitic microstructures after the CA heat treatment is different from the as-built microstructures that have undergone primarily diffusional transformations instead (Figs. 7, 8). The strong preference toward the (100) plane for the as-built conditions align with expectations that the solidification microstructure (i.e., $\delta$-ferrite) is influenced by the strong thermal gradient direction from the melt pool promoting growth in the < 100 > direction. The preferred orientation along the (101) planes in the CA builds is due to the martensitic microstructure in which the transformation constraints determine the habit planes [70].

For the as-built condition, it can be observed that the grain boundary plane distribution for the low energy 60°/[111] intervariant boundaries has a diffuse peak at the low energy near twist {102} orientations which is close to the distribution reported in polygonal ferrite microstructures [71, 72]. On the other hand, the martensitic microstructures show a distinct peak at the {110} twist plane orientations which is in accordance with what has been previously observed in wrought martensitic 17-4 PH steels [40]. It should be noted that according to the crystallography of the K–S orientation relationship, the close packed planes of the austenite phase should be parallel to the close packed planes of the martensite imposing impingement of the variant at the higher energy twist {110} plane orientations. Therefore, the crystallographic constraints associated with the phase transformation mostly govern the boundary characteristics during the CA treatment, while the as-built microstructures mostly follow the configurations promoted by solidification and texture.

### *Impact of composition and austenite microstructure on variant selection*

The intervariant boundary populations are generally sensitive to various factors, including chemical composition [40, 73, 74], phase transformation mechanisms [75], crystallographic texture [76], temperature [77], strain [54], and grain size [78]. Here, the effect of phase transformation pathways and crystallographic texture can be excluded as contributing factors, mainly due to both builds undergoing martensitic transformations governed by the K–S orientation relationship, resulting in similar transformation texture characteristics [79]. Based on the austenite reconstruction, both builds show weak textures around the < 111 > or < 110 > directions dependent on the collected dataset for both High N and Low N builds. As these textures are relatively weak, they will not have a strong impact on the grain boundary population. That leaves chemical composition, the phase transformation temperature, and grain size as potential factors. The martensite transformation occurs through variant selection that is dictated by the associated shape strain development and the involved accommodation mechanisms (i.e., slip and twinning). The transformation strain is accommodated by the formation of specific variant arrangements (i.e., variant selection), resulting in specific intervariant network characteristics in the microstructure. Which of the slip or twinning mechanisms is developed during the transformation is strongly associated with the lattice parameters of the parent and daughter phases [80, 81].

The $\delta$-ferrite to austenite transformation kinetics and initial as-built $\delta$-ferrite grain structure will play a large role in influencing the transformation of austenite to martensite after the CA heat treatment. The higher density of grain boundaries in combination with the lower barrier to nucleation in the High N builds, as discussed previously, results in a significantly higher number of austenite grains in the High N builds [82]. The resulting transformation path (i.e., austenite to martensite) is impacted twofold based on the parent austenite structure. Firstly, the parent grain size alters the martensite start ($M_s$) and martensite finish ($M_f$) temperatures [34, 38]. Such a change in the martensite transformation temperatures likely plays a role in the stabilization of austenite in High N builds after the CA heat treatment (Fig. 3). Previous studies have reported that the $M_s$ temperature starts to decrease at parent austenite grain diameters below ~ 10 μm [37]. As the reconstructed parent austenite grains in the High N samples have a mean grain diameter of ~ 10.2 ± 0.4 μm (Fig. 3), there is a high likelihood that the size of a subsection of grains results in the suppression of the $M_s$ temperature. This is different to the Low N builds which have a mean reconstructed PAGS of ~ 52.6 ± 0.1 μm.

Second, the parent austenite grain structure has an impact on the variant selection of martensite. Martensite forms in multi-variant blocks to minimize the volume expansion that accompanies the martensitic transformations. A smaller PAGS limits the number of variants that can form within a single austenite grain, ultimately changing the intervariant boundary population [34, 40]. Parent austenite grain refinement will alter the misorientation angle distribution, resulting in an increased population of non-K–S misorientations ranging from 23° to 45° and a decrease in the population of K–S-related boundaries with misorientations in the range 10°–22° and 46°–60° (as can be seen in Fig. 5). The reduction in the number of K–S related boundaries is mainly related to the intersection of variants belonging to two neighboring parent austenite grains with distinct orientations. The impact of the PAGS is consistent with the High N build showing a decrease in populations of 60°/$[1\,1\,\bar{1}]$, 10.5°/$[0\,\bar{1}\,\bar{1}]$ and 10.5°/$[1\,1\,\bar{1}]$ boundaries and increase in populations of 60°/$[0\,1\,1]$, 14.9°/$[13\,5\,1]$, 57.21°/$[\bar{6}\,\bar{2}\,5]$, and 51.7°/ $[\overline{11}\,6\,\overline{11}]$ (Fig. 7). However, the fraction of retained austenite and changes in the intervariant boundary network requires us to also consider the differences in the chemical composition of the High N and Low N builds which result in notable changes in lattice sizes of the phases, impacting the transformation to martensite.

Composition has a similar impact as the PAGS in that it can influence both the martensite transformation temperature and the variant selection. Considering the retained austenite within the microstructure of the High N builds, the increase in N content has the impact of decreasing the $M_s$ and $M_f$ temperatures and makes the occurrence of retained austenite more likely [83, 84]. It should be noted, however, that the influence of either the composition or the PAGS on the retained austenite cannot be easily deconvoluted, thus, a statement on either contributing factor cannot be made here.

The impact of composition on variant selection is primarily exhibited through alteration of the lattice parameters of the parent austenite and martensite phases. Variations in lattice distortion and inhomogeneous shear during the phase transformation are caused by this difference in lattice correspondence between the austenite and martensite phases [40]. The martensitic phase transformation mechanism (i.e., dislocation slip vs. twinning) can then be controlled, allowing for the development of unique variant selection arrangements that can better accommodate the strain introduced by the transformation [85]. The austenite lattice parameters decreased from 3.5961 to 3.591 Å from the High N to the Low N builds, and for martensite from 2.8729 to 2.8699 Å from the High N to Low N builds, respectively. It should be noted that the XRD peaks related to the Low N builds did not exhibit any austenite peaks; therefore, austenite lattice parameters were taken from [40], whereas the other ones were calculated from our XRD data (in Fig. 3). The change in lattice parameter influences the elastic strain associated with the shear/displacive transformation, potentially influencing variant arrangement. To evaluate the impact of lattice parameter and the associated change in elastic strain, the phenomenological theory of martensite crystallography (PTMC), that considers the lattice parameter of both parent austenite and martensite for High N and Low N parent austenite grains, was employed. Greater detail on PTMC is given in Section S1 in the supplementary materials and in [86–91].

The combination of different variant arrangements calculated using PTMC is shown in Table 4. The change in chemical composition between the different powder manufactures influences the respective austenite and martensite lattice parameters, ultimately affecting the inhomogeneous shear magnitude (supplementary Table S2). However, the shear magnitude is not significantly different between different variant combinations for each composition, indicating that all combinations have almost a similar probability to form within a parent austenite grain. To better compare the combination of variants between the two builds, the overall probability of various intervariants for all the possible combinations is also calculated (Table 4). It can be observed that the 60°/[1 1 0] intervariant boundaries have about a 50% formation probability from the possible combinations promoted during the martensitic phase transformation. In comparison, the variant combination in the Low N builds show formation probabilities of 33% and 30% for 60°/[1 1 0] and 60°/[1 1 1] intervariants, respectively. This is consistent with the measured intervariant boundary population distribution of both builds after the CA treatment (Fig. 7), where the population of 60°/[1 1 0] boundaries increases at the expense of 60°/[1 1 1] in High N composition in comparison with the Low N composition. It should be mentioned that the minimum shear strain for all variant combinations is close, therefore, no tendency for specific variant arrangements can be expected in the microstructure of either build.

The results of the PTMC calculations are consistent with the variant arrangements observed in the microstructure of Low N and High N alloys (Fig. 7) showing how composition (i.e., increased concentrations of N) not only impacts the nucleation of austenite, but also the variant selection within martensite. Nevertheless, it should be noted that other variation arrangements, which may not have the lowest strain according to the PTMC (Table 4), can also be observed in the microstructures. The observed mismatch may be attributed, in part, to the limitations of two-dimensional observations, which fail to adequately capture the three-dimensional configuration of variants. Furthermore, it should be noted that the strain variation among various variant arrangements is found to be below 5% according to the data presented in Table 4. This finding suggests the potential for the formation of alternative variant configurations inside certain grains.

### *Connectivity of intervariant boundaries in as-built and CA builds*

Both the PTMC calculation and the observation of different variant groups support the finding that the High N composition in conjunction with reduced parent austenite grain size results in a higher occurrence of 60°/[1 1 0] intervariant boundaries, while reducing the occurrence of intervariant boundaries with 60°/[1 1 $\bar{1}$] misorientations. The change in variant arrangements (variant selection mechanism) resulting from the change in the composition and

**Table 4** Equivalent strains associated with von Mises criteria for different combinations of variant cluster arrangements in the Low N and High N samples subjected to martensitic transformation

| Condition | Low N | | | | High N | | | |
|---|---|---|---|---|---|---|---|---|
| | Min $\varepsilon$ | Variant combination | Possible intervariants | | Min $\varepsilon$ | Variant combination | Possible intervariants | |
| | | | Axis/angle | Probability (%) | | | Axis/angle | Probability (%) |
| 2-Variant | 0.0673 | V1V2 | 60°/[111] | 100 | 0.0663 | V1V3 | 60°/[110] | 100 |
| 3-Variant | 0.0639 and 0.0605 | V1V2V5 and V1V2V6 | 60°/[111] | 33 | 0.0638 and 0.0634 | V1V3V5 and V1V2V5 | 60°/[110] | 75 |
| | | | 60°/[011] | 33 | | | | |
| | | | 10.5°/$[0\,\overline{11}]$ | 16 | | | | |
| | | | 49.5°/[011] | 16 | | | 60°/[111] | 25 |
| 4-Variant | 0.631 | V1V2V3V5 | 60°/[111] | 29 | 0.632 | V1V2V3V5 | 60°/[111] | 29 |
| | | | 60°/[011] | 43 | | | 60°/[011] | 43 |
| | | | 10.5°/$[0\,\overline{11}]$ | 14 | | | 10.5°/$[0\,\overline{11}]$ | 14 |
| | | | 49.5°/[011] | 14 | | | 49.5°/[011] | 14 |
| 5-Variant | 0.0606 and 0.0616 | V1V2V3V4V5 and V1V2V3V4V6 | 60°/[111] | 30 | 0.0607 and 0.0615 | V1V2V3V4V5 and V1V2V3V4V6 | 60°/[111] | 30 |
| | | | 60°/ [011] | 38 | | | 60°/[011] | 38 |
| | | | 10.5°/$[0\,\overline{11}]$ | 23 | | | 10.5°/$[0\,\overline{11}]$ | 23 |
| | | | 49.5°/[011] | 8 | | | 49.5°/[011] | 8 |
| All combinations | | | 60°/[111] | 33 | | | 60°/[111] | 27 |
| | | | 60°/[011] | 30 | | | 60°/[011] | 50 |
| | | | 10.5°/$[0\,\overline{11}]$ | 16 | | | 10.5°/$[0\,\overline{11}]$ | 15 |
| | | | 49.5°/[011] | 10 | | | 49.5°/[011] | 7 |

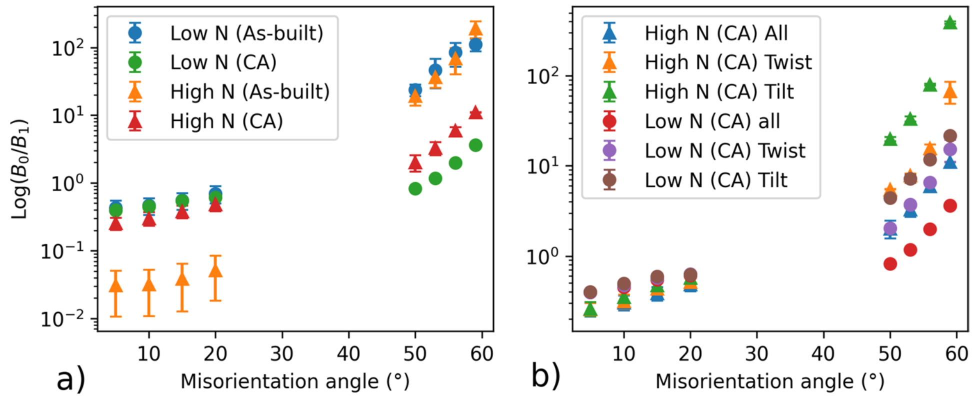


**Figure 12** Inverse connectivity of the boundary network as a function of misorientation angle threshold for **a** all boundaries of the as-built and CA heat treated samples and, **b** different {1 1 0} boundaries (tilt and twist) of CA samples of Low and High N builds.

PAGS can also impact the connectivity of intervariant boundaries. The enhancement of the connectivity of the low energy intervariant boundaries reduces their boundary spacings, and impedes the dislocation movement and coalescence of voids [37]. Here, a homology metric approach [92, 93] was used to measure the connectivity of the boundaries (Fig. 12). For each EBSD map of the low and High N alloys, the topology parameters (Betti numbers) $B_0$ and $B_1$ are measured. The parameter $B_1$ refers to the closed paths and continuous boundaries, while the $B_0$ refers to isolated boundary segments within the microstructure. The inverse connectivity of the boundary network can be characterized by $B_0/B_1$, known as $B_{01}$, within a given microstructure [40, 70]. Therefore, the enhanced connectivity of interest will be reflected in lower $B_0/B_1$ values. Here, the connectivity of the intervariant boundaries was calculated using the CHOMP software for K–S related misorientation angles (excluding 23°–45° misorientations).

The grain boundary network connectivity clearly shows a distinct difference between the as-built microstructures (ferritic) and the CA heat treated (martensitic) microstructures. Generally, the connectivity of the martensitic microstructure is significantly higher compared to the ferritic microstructure at high-angle boundaries ($\theta$> 45°, Fig. 12a). These changes reflect the distinct difference in the misorientation angle distribution of these microstructures (Fig. 5). Comparison of the Low N and High N CA builds, however, reveals a slightly lower connectivity for the Low N CA builds compared to the High N CA build.

The connectivity of the intervariant boundaries at a given crystallographic plane can also be observed in Fig. 12b for the CA builds. Here, the interfaces of the K–S orientation relationship are mostly terminated on the {1 1 0} or near {1 1 0} planes, therefore, by extracting the K–S related misorientation angles, the connectivity of all the {1 1 0} planes can be measured. In parallel, with further considering the [1 1 1] and [1 1 0] misorientation axes related to the K–S orientation relationship, the connectivity can be measured based on the {1 1 0} symmetric tilt and twist-type boundaries, respectively. In general, at low-angle threshold, the {1 1 0} boundary planes share a similar connectivity with the tilt and twist character boundaries. However, with the increase in the misorientation angle threshold, the inverse boundary network connectivity (B0/B1 value) increases for all conditions.

The Low N {1 1 0} boundaries show a greater connectivity compared to the High N boundaries (Fig. 12b). Interestingly, the tilt and twist character boundaries for the Low N condition have similar connectivity values, mostly due to the similar distribution of 60°/[1 1 1] and 60°/[1 1 0] boundaries (Fig. 7). However, the {110} tilt boundaries show the least connectivity compared to the {1 1 0} twist character boundaries in the High N alloy (Fig. 12b). This reduction in connectivity of tilt boundaries can be attributed to a decrease in the occurrence of 60°/[1 1 1] boundaries (Fig. 7). In all scenarios, a higher population of a specific grain boundary type increases the probability of their intersection and the subsequent formation of a more interconnected network.

## Conclusions

We systematically studied the microstructural evolution of two 17-4 PH L-PBF builds (High N versus Low N) in their as-built state and its impact on the final martensitic microstructure after the standard solution annealing and quenching (CA) heat treatment. Our results demonstrate the extreme sensitivity of 17-4 PH in producing different martensitic microstructures in the CA state due to different initial as-built microstructures and the associated differences in the L-PBF processing parameters and powder compositions. Overall, the following conclusions can be obtained from this work:

- Upon solidification, both builds formed a predominately $\delta$-ferrite microstructure in their as-built conditions. In the High N build, a low fraction of small austenite grains formed. The difference in $\delta$-ferrite grain size was attributed to the difference in solidification conditions and confirmed through computational analysis via thermal simulations. The difference in density of $\delta$-ferrite grain boundaries and the fraction of high-angle grain boundaries was also attributed to a difference in PAGS between the Low N and High N builds.
- The PAGS had an impact on the final martensitic microstructure through two factors. The first is through effecting the $M_s$ temperature. With a decrease in austenite grain size, $M_s$ decreases. The decrease in $M_s$ temperature in the smaller grains likely led to the increase in the retained austenite grains in the High N builds which averaged in diameter around ~ $10.2 \pm 0.4$ µm. Second, the austenite grain size influences the variant selection due to size constraints induced by the austenite grains and due to the decreasing $M_s$ temperature. This influences the elastic strain associated with the shear/displacive transformation of the martensite transformation.
- The impact of the powder composition on the martensitic microstructure is seen through increases in the amount of retained austenite and through altering the austenite and martensite lattice parameters. The change in lattice parameter influences the elastic strain associated with the shear/displacive transformation, thus influencing variant arrangement.
- It is shown that an increase in connectivity between martensite grain boundaries occurs going from the Low N CA to the High N CA builds, where an increase in connectivity is associated with an increase in toughness. However, it was noted that the high fraction of retained austenite in the High N CA builds would likely negatively impact their mechanical properties, thus, showing the importance of controlling the parent austenite grain size.

These results demonstrate that universal standards cannot be made easily, and decisions on processing parameters and heat treatments will have to be made with considerations of powder composition's impact on the final microstructure. Further, the additive manufacturing process was shown to have influence over an often-overlooked microstructural feature of martensitic steels, the interface characteristics, which are expected to play a role in controlling the properties of the material.

## Acknowledgements

Financial supports by the Department of Industry, Innovation and Science, Australia via the AUSMURI program and the Australian Research Council Discovery scheme (AUSMURI000005, DP230101063) are acknowledged. The authors acknowledge the facilities, scientific, and technical support provided at the Electron Microscope Unit, UNSW Sydney (Mark Wainwright Analytical Centre), a node of Microscopy Australia, a national research facility supported under the Commonwealth NCRIS program. The authors also acknowledge the facilities, as well as the scientific and technical support of the Sydney Manufacturing Hub (SMH) at the University of Sydney. The authors thank Dr. Maxwell Moyle at UNSW Sydney for support with the EBSD analyses. The authors acknowledge Prof. Gregory Rohrer at Carnegie Mellon University, USA, for kindly providing us with their GBCD codes.

## Author contributions

Michael P Haines involved in conceptualization, methodology, formal analysis, investigation, writing—original draft, and data curation; Ehsan Farabi involved in conceptualization, methodology, formal analysis, investigation, and writing—review and editing; Nima Haghdadi involved in conceptualization, methodology, resources, writing—review and editing, supervision, and funding acquisition; Sophie Primig involved in conceptualization, methodology, resources, writing—review and editing, supervision, project administration, and funding acquisition.

## Funding

Open Access funding enabled and organized by CAUL and its Member Institutions. Defence Science and Technology Group, AUSMURI000005, Australian Research Council, DP230101063.

## Data availability

These will be made available upon reasonable request.

## Declarations

**Ethical approval** Not applicable.

**Supplementary Information** The online version contains supplementary material available at https://doi.org/10.1007/s10853-025-10645-8.



## References

[1] Gokcekaya O, Ishimoto T, Hibino S, Yasutomi J, Narushima T, Nakano T (2021) Unique crystallographic texture formation in Inconel 718 by laser powder bed fusion and its effect on mechanical anisotropy. Acta Mater 212:116876. https://doi.org/10.1016/j.actamat.2021.116876

[2] Frederick CL, Plotkowski A, Kirka MM, Haines M, Staub A, Schwalbach EJ, Cullen D, Babu SS (2018) Geometry-induced spatial variation of microstructure evolution during selective electron beam melting of rene-N5. Metall Mater Trans A 49(10):5080–5096. https://doi.org/10.1007/s11661-018-4793-y

[3] Moyle MS, Haghdadi N, Liao XZ, Ringer SP, Primig S (2022) On the microstructure and texture evolution in 17-4 PH stainless steel during laser powder bed fusion: towards textural design. J Mater Sci Technol 117:183–195. https://doi.org/10.1016/j.jmst.2021.12.015

[4] Sofinowski KA, Raman S, Wang X, Gaskey B, Seita M (2021) Layer-wise engineering of grain orientation (LEGO) in laser powder bed fusion of stainless steel 316L. Addit Manuf 38:101809. https://doi.org/10.1016/j.addma.2020.101809

[5] Plotkowski A, Ferguson J, Stump B, Halsey W, Paquit V, Joslin C, Babu SS, Marquez Rossy A, Kirka MM, Dehoff RR (2021) A stochastic scan strategy for grain structure control in complex geometries using electron beam powder bed fusion. Addit Manuf 46:102092. https://doi.org/10.1016/j.addma.2021.102092

[6] Halsey W, Ferguson J, Plotkowski A, Dehoff R, Paquit V (2020) Geometry-independent microstructure optimization for electron beam powder bed fusion additive manufacturing. Addit Manuf 35:101354. https://doi.org/10.1016/j.addma.2020.101354

[7] Raplee J, Plotkowski A, Kirka MM, Dinwiddie R, Okello A, Dehoff RR, Babu SS (2017) Thermographic microstructure monitoring in electron beam additive manufacturing. Sci Rep 7:1–16. https://doi.org/10.1038/srep43554

[8] Rolchigo M, Coleman J, Knapp GL, Plotkowski A (2024) Grain structure and texture selection regimes in metal powder bed fusion. Addit Manuf 81:104024. https://doi.org/10.1016/j.addma.2024.104024

[9] Hsiao CN, Chiou CS, Yang JR (2002) Aging reactions in a 17-4 PH stainless steel. Mater Chem Phys 74:134–142. https://doi.org/10.1016/S0254-0584(01)00460-6

[10] Murr LE, Martinez E, Hernandez J, Collins S, Amato KN, Gaytan SM, Shindo PW (2012) Microstructures and properties of 17-4 PH stainless steel fabricated by selective laser melting. J Mater Res Technol 1:167–177. https://doi.org/10.1016/S2238-7854(12)70029-7

[11] Bhambroo R, Roychowdhury S, Kain V, Raja VS (2013) Effect of reverted austenite on mechanical properties of precipitation hardenable 17-4 stainless steel. Mater Sci Eng A 568:127–133. https://doi.org/10.1016/j.msea.2013.01.011

[12] Lin X, Cao Y, Wu X, Yang H, Chen J, Huang W (2012) Microstructure and mechanical properties of laser forming repaired 17-4PH stainless steel. Mater Sci Eng A 553:80–88. https://doi.org/10.1016/j.msea.2012.05.095

[13] Arisoy CF, Başman G, Şeşen MK (2003) Failure of a 17-4 PH stainless steel sailboat propeller shaft. Eng Fail Anal 10:711–717. https://doi.org/10.1016/S1350-6307(03)00041-4

[14] Kultz Unti LF, Aota LS, Jardini AL, Tschiptschin AP, Sandim HRZ, Jägle EA, Zilnyk KD (2021) Microstructural characterization of 15-5PH stainless steel processed by laser powder-bed fusion. Mater Charact 181:111485. https://doi.org/10.1016/j.matchar.2021.111485

[15] Alnajjar M, Christien F, Wolski K, Bosch C (2019) Evidence of austenite by-passing in a stainless steel obtained from laser melting additive manufacturing. Addit Manuf 25:187–195. https://doi.org/10.1016/j.addma.2018.11.004

[16] Sun Y, Hebert RJ, Aindow M (2020) Effect of laser scan length on the microstructure of additively manufactured 17-4PH stainless steel thin-walled parts. Addit Manuf 35:101302. https://doi.org/10.1016/j.addma.2020.101302

[17] Meredith SD, Zuback JS, Keist JS, Palmer TA (2018) Impact of composition on the heat treatment response of additively manufactured 17-4 PH grade stainless steel. Mater Sci Eng A 738:44–56. https://doi.org/10.1016/j.msea.2018.09.066

[18] Irrinki H, Nath SD, Alhofors M, Stitzel J, Gulsoy O, Atre SV (2019) Microstructures, properties, and applications of laser sintered 17-4PH stainless steel. J Am Ceram Soc 102:5679–5690. https://doi.org/10.1111/jace.16372

[19] Yadollahi A, Shamsaei N, Thompson SM, Elwany A, Bian L (2017) Effects of building orientation and heat treatment on fatigue behavior of selective laser melted 17-4 PH stainless steel. Int J Fatigue 94:218–235. https://doi.org/10.1016/j.ijfatigue.2016.03.014

[20] Nezhadfar PD, Anderson-Wedge K, Daniewicz SR, Phan N, Shao S, Shamsaei N (2020) Improved high cycle fatigue performance of additively manufactured 17-4 PH stainless steel via in-process refining micro-/defect-structure. Addit Manuf 36:101604. https://doi.org/10.1016/j.addma.2020.101604

[21] Vunnam S, Saboo A, Sudbrack C, Starr TL (2019) Effect of powder chemical composition on the as-built microstructure of 17-4 PH stainless steel processed by selective laser melting. Addit Manuf 30:100876. https://doi.org/10.1016/j.addma.2019.100876

[22] Sabooni S, Chabok A, Feng SC, Blaauw H, Pijper TC, Yang HJ, Pei YT (2021) Laser powder bed fusion of 17-4 PH stainless steel: a comparative study on the effect of heat treatment on the microstructure evolution and mechanical properties. Addit Manuf 46:102176. https://doi.org/10.1016/j.addma.2021.102176

[23] Sun Y, Hebert RJ, Aindow M (2018) Effect of heat treatments on microstructural evolution of additively manufactured and wrought 17-4PH stainless steel. Mater Des 156:429–440. https://doi.org/10.1016/j.matdes.2018.07.015

[24] Yeon S, Yoon J, Kim TB, Lee SH, Jun T, Son Y, Choi K (2022) Normalizing effect of heat treatment processing on 17-4 PH stainless steel manufactured by powder bed fusion. Metals (Basel) 12:704. https://doi.org/10.3390/met12050704

[25] Li K, Zhan J, Yang T, To AC, Tan S, Tang Q, Cao H, Murr LE (2022) Homogenization timing effect on microstructure and precipitation strengthening of 17-4PH stainless steel fabricated by laser powder bed fusion. Addit Manuf 52:102672. https://doi.org/10.1016/j.addma.2022.102672

[26] Shi Q, Qin F, Li K, Liu X, Zhou G (2021) Effect of hot isostatic pressing on the microstructure and mechanical properties of 17-4PH stainless steel parts fabricated by selective laser melting. Mater Sci Eng A 810:141035. https://doi.org/10.1016/j.msea.2021.141035

[27] Wang XL, Wang ZQ, Dong LL, Shang CJ, Ma XP, Subramanian SV (2017) New insights into the mechanism of cooling rate on the impact toughness of coarse grained heat affected zone from the aspect of variant selection. Mater Sci Eng A 704:448–458. https://doi.org/10.1016/j.msea.2017.07.095

[28] Guo Z, Lee CS, Morris JW (2004) On coherent transformations in steel. Acta Mater 52:5511–5518. https://doi.org/10.1016/j.actamat.2004.08.011

[29] Haghdadi N, Laleh M, Kosari A, Moayed MH, Cizek P, Hodgson PD, Beladi H (2019) The effect of phase transformation route on the intergranular corrosion susceptibility of 2205 duplex stainless steel. Mater Lett 238:26–30. https://doi.org/10.1016/j.matlet.2018.11.143

[30] Haghdadi N, Laleh M, Chen H, Chen Z, Ledermueller C, Liao X, Ringer S, Primig S (2021) On the pitting corrosion of 2205 duplex stainless steel produced by laser powder bed fusion additive manufacturing in the as-built and post-processed conditions. Mater Des 212:110260. https://doi.org/10.1016/j.matdes.2021.110260

[31] Laleh M, Hughes AE, Xu W, Haghdadi N, Wang K, Cizek P, Gibson I, Tan MY (2019) On the unusual intergranular corrosion resistance of 316L stainless steel additively manufactured by selective laser melting. Corros Sci 161:108189. https://doi.org/10.1016/j.corsci.2019.108189

[32] Haghdadi N, Cizek P, Hodgson PD, Beladi H (2019) Microstructure dependence of impact toughness in duplex

stainless steels. Mater Sci Eng A 745:369–378. https://doi.org/10.1016/j.msea.2018.12.117

[33] Liu M, Liu Y, Li H (2022) Deformation mechanism of ferrite in a low carbon Al-killed steel: slip behavior, grain boundary evolution and GND development. Mater Sci Eng A 842:143093. https://doi.org/10.1016/j.msea.2022.143093

[34] Hanamura T, Torizuka S, Tamura S, Enokida S, Takechi H (2013) Effect of austenite grain size on transformation behavior, microstructure and mechanical properties of 0.1C–5Mn martensitic steel. ISIJ Int 53(12):2218–2225. https://doi.org/10.2355/isijinternational.53.2218

[35] Takaki S, Fukunaga K, Syarif J, Tsuchiyama T (2004) Effect of grain refinement on thermal stability of metastable austenitic steel. Mater Trans 45:2245–2251. https://doi.org/10.2320/matertrans.45.2245

[36] Yang HS, Bhadeshia HKDH (2009) Austenite grain size and the martensite-start temperature. Scr Mater 60:493–495. https://doi.org/10.1016/j.scriptamat.2008.11.043

[37] Mirzaei A, Hodgson PD, Ma X, Peterson VK, Farabi E, Rohrer GS, Beladi H (2024) The role of parent austenite grain size on the variant selection and intervariant boundary network in a lath martensitic steel. Mater Sci Eng A 889:145793. https://doi.org/10.1016/j.msea.2023.145793

[38] Archie F, Zaefferer S (2018) On variant selection at the prior austenite grain boundaries in lath martensite and relevant micro-mechanical implications. Mater Sci Eng A 731:539–550. https://doi.org/10.1016/j.msea.2018.06.090

[39] Gourgues AF, Flower HM, Lindley TC (2000) Electron backscattering diffraction study of acicular ferrite, bainite, and martensite steel microstructures. Mater Sci Technol 16:26–40. https://doi.org/10.1179/026708300773002636

[40] Govindaraj V, Farabi E, Kada S, Hodgson PD, Singh RP, Rohrer GS, Beladi H (2021) Effect of manganese on the grain boundary network of lath martensite in precipitation hardenable stainless steels. J Alloys Compd 886:161333. https://doi.org/10.1016/j.jallcom.2021.161333

[41] A705/A705M, Specification for Age-Hardening Stainless Steel Forgings (2023). https://doi.org/10.1520/A0705_A0705M-23

[42] Cheruvathur S, Lass EA, Campbell CE (2016) Additive manufacturing of 17-4 PH stainless steel: post-processing heat treatment to achieve uniform reproducible microstructure. Jom 68:930–942. https://doi.org/10.1007/s11837-015-1754-4

[43] LeBrun T, Nakamoto T, Horikawa K, Kobayashi H (2015) Effect of retained austenite on subsequent thermal processing and resultant mechanical properties of selective laser melted 17-4 PH stainless steel. Mater Des 81:44–53. https://doi.org/10.1016/j.matdes.2015.05.026

[44] Ranger C, Tari V, Farjami S, Merwin MJ, Germain L, Rollett A (2018) Austenite reconstruction elucidates prior grain size dependence of toughness in a low alloy steel. Metall Mater Trans A 49(10):4521–4535. https://doi.org/10.1007/s11661-018-4825-7

[45] Rohrer GS, Saylor DM, El Dasher B, Adams BL, Rollett AD, Wynblatt P (2004) The distribution of internal interfaces in polycrystals. Z Met 95(4):197–214. https://doi.org/10.3139/146.017934

[46] Plotkowski A, Rios O, Sridharan N, Sims Z, Unocic K, Ott RT, Dehoff RR, Babu SS (2017) Evaluation of an Al–Ce alloy for laser additive manufacturing. Acta Mater 126:507–519. https://doi.org/10.1016/j.actamat.2016.12.065

[47] Stump B, Plotkowski A (2019) An adaptive integration scheme for heat conduction in additive manufacturing. Appl Math Model 75:787–805. https://doi.org/10.1016/j.apm.2019.07.008

[48] Nandwana P, Plotkowski A, Kannan R, Yoder S, Dehoff R (2020) Predicting geometric influences in metal additive manufacturing. Mater Today Commun 25:101174. https://doi.org/10.1016/j.mtcomm.2020.101174

[49] Plotkowski A, Pries J, List F, Nandwana P, Stump B, Carver K, Dehoff RR (2019) Influence of scan pattern and geometry on the microstructure and soft-magnetic performance of additively manufactured Fe–Si. Addit Manuf 29:100781. https://doi.org/10.1016/j.addma.2019.100781

[50] Nguyen NT, Ohta A, Matsuoka K, Suzuki N, Maeda Y (1999) Analytical solutions for transient temperature of semi-infinite body subjected to 3-D moving heat sources. Weld J 78:265–274

[51] Sabau AS, Porter WD (2008) Alloy shrinkage factors for the investment casting of 17-4PH stainless steel parts. Metall Mater Trans B 39(2):317–330. https://doi.org/10.1007/s11663-007-9125-3

[52] Kurdjumow G, Sachs G (1930) Over the mechanisms of steel hardening. Zeitschrift Für Phys 18:534–534. https://doi.org/10.1007/BF01513427

[53] Sonderegger B, Mitsche S, Cerjak H (2007) Martensite laths in creep resistant martensitic 9–12% Cr steels—calculation and measurement of misorientations. Mater Charact 58:874–882. https://doi.org/10.1016/j.matchar.2006.08.014

[54] Beladi H, Rohrer GS (2017) The role of thermomechanical routes on the distribution of grain boundary and interface plane orientations in transformed microstructures. Metall Mater Trans A 48(6):2781–2790. https://doi.org/10.1007/s11661-016-3630-4

[55] Glowinski K, Morawiec A (2012) A toolbox for geometric grain boundary characterization. 1st Int Conf 3D Mater Sci, 3DMS. 119–124

[56] Frederick CL (2018) Control of Grain Structure in Selective-Electron Beam Melting of Nickel-based Superalloys, University of Tennessee. https://trace.tennessee.edu/utk_graddiss/4952.

[57] Foster SJ, Carver K, Dinwiddie RB, List F, Unocic KA, Chaudhary A, Babu SS (2018) Process-defect-structure-property correlations during laser powder bed fusion of alloy 718: role of in situ and ex situ characterizations. Metall Mater Trans A 49(11):5775–5798. https://doi.org/10.1007/s11661-018-4870-2

[58] Raghavan N, Dehoff R, Pannala S, Simunovic S, Kirka MM, Turner J, Carlson N, Babu SS (2016) Numerical modeling of heat-transfer and the influence of process parameters on tailoring the grain morphology of IN718 in electron beam additive manufacturing. Acta Mater 112:303–314. https://doi.org/10.1016/j.actamat.2016.03.063

[59] Babu SS (2009) Thermodynamic and kinetic models for describing microstructure evolution during joining of metals and alloys. Int Mater Rev 54:333–367. https://doi.org/10.1179/095066009X12506720908654

[60] Haines M, Plotkowski A, Frederick CL, Schwalbach EJ, Babu SS (2018) A sensitivity analysis of the columnar-to-equiaxed transition for Ni-based superalloys in electron beam additive manufacturing. Comput Mater Sci 155:340–349. https://doi.org/10.1016/j.commatsci.2018.08.064

[61] Dantzig JA, Rappaz M (2009) Solidification. CRC Press, Fl, Boca Raton

[62] Hunt JD (1984) Steady state columnar and equiaxed growth of dendrites and eutectic. Mater Sci Eng 65:75–83. https://doi.org/10.1016/0025-5416(84)90201-5

[63] Raghavan N, Simunovic S, Dehoff R, Plotkowski A, Turner J, Kirka M, Babu S (2017) Localized melt-scan strategy for site specific control of grain size and primary dendrite arm spacing in electron beam additive manufacturing. Acta Mater 140:375–387. https://doi.org/10.1016/j.actamat.2017.08.038

[64] Singh KK, Moridi A (2023) Metastability mediated grain size control in PH 17-4 stainless steel fabricated using laser-powder bed fusion (LPBF). Materialia 30:101857. https://doi.org/10.1016/j.mtla.2023.101857

[65] Shaffer DJ, Wilson-Heid AE, Keist JS, Beese AM, Palmer TA (2021) Impact of retained austenite on the aging response of additively manufactured 17-4 PH grade stainless steel. Mater Sci Eng A 817:141363. https://doi.org/10.1016/j.msea.2021.141363

[66] Moyle MS, Haghdadi N, Theska F, Haines MP, Liao XZ, Ringer SP, Primig S (2024) Effect of compositional variations on the heat treatment response in 17-4 PH stainless steel fabricated by laser powder bed fusion. Mater Charact 209:113768. https://doi.org/10.1016/j.matchar.2024.113768

[67] Lange WF, Enomoto M, Aaronson HI (1989) Precipitate nucleation kinetics at grain boundaries. Int Mater Rev 34:125. https://doi.org/10.1179/imr.1989.34.1.125

[68] Morris JW Jr, Guo Z, Krenn CR, Kim Y-H (2001) Advances in physical metallurgy and processing of steels. The limits of strength and toughness in steel. ISIJ Int 41(6):599–611. https://doi.org/10.2355/isijinternational.41.599

[69] Shibata A, Takahashi H, Tsuji N (2012) Microstructural and crystallographic features of hydrogenrelated crack propagation in low carbon martensitic steel. ISIJ Int 52:208–212. https://doi.org/10.2355/isijinternational.52.208

[70] Beladi H, Rohrer GS, Rollett AD, Tari V, Hodgson PD (2014) The distribution of intervariant crystallographic planes in a lath martensite using five macroscopic parameters. Acta Mater 63:86–98. https://doi.org/10.1016/j.actamat.2013.10.010

[71] Beladi H, Rohrer GS (2013) The relative grain boundary area and energy distributions in a ferritic steel determined from three-dimensional electron backscatter diffraction maps. Acta Mater 61:1404–1412. https://doi.org/10.1016/j.actamat.2012.11.017

[72] Beladi H, Rohrer GS (2013) The distribution of grain boundary planes in interstitial free steel. Metall Mater Trans A 44(1):115–124. https://doi.org/10.1007/s11661-012-1393-0

[73] Randle V (1999) Mechanism of twinning-induced grain boundary engineering in low stacking-fault energy materials. Acta Mater 47:4187–4196. https://doi.org/10.1016/S1359-6454(99)00277-3

[74] Randle V (1998) Refined approaches to the use of the coincidence site lattice. Jom 50:56–59. https://doi.org/10.1007/s11837-998-0251-4

[75] Haghdadi N, Cizek P, Hodgson PD, Tari V, Rohrer GS, Beladi H (2018) Effect of ferrite-to-austenite phase transformation path on the interface crystallographic character distributions in a duplex stainless steel. Acta Mater 145:196–209. https://doi.org/10.1016/j.actamat.2017.11.057

[76] Moyle M, Ledermueller C, Zou Z, Primig S, Haghdadi N (2022) Multi-scale characterisation of microstructure and texture of 316L stainless steel manufactured by laser powder bed fusion. Mater Charact 184:111663. https://doi.org/10.1016/j.matchar.2021.111663

[77] Schwartz AJ, King WE, Kumar M (2006) Influence of processing method on the network of grain boundaries. Scr Mater 54:963–968. https://doi.org/10.1016/j.scriptamat.2005.11.052

[78] Liu T, Xia S, Li H, Zhou B, Bai Q, Su C, Cai Z (2013) Effect of initial grain sizes on the grain boundary network during grain boundary engineering in Alloy 690. J Mater Res 28:1165–1176. https://doi.org/10.1557/jmr.2013.37

[79] Ray RK, Jonas JJ (1990) Transformation textures in steels. Int Mater Rev 35:1–36. https://doi.org/10.1179/095066090790324046

[80] Miyazaki S, Otsuka K, Wayman CM (1989) The shape memory mechanism associated with the martensitic transformation in Ti–Ni alloys—I. Self-accommodation. Acta Met 7:1873–1884

[81] Otsuka K, Wayman C (1998) Mechanism of shape memory effect and superelasticity. Shape Mem Mater 27–48

[82] Humphreys FJ, Hatherly M (1995) Recrystallization textures. Recrystallization and related annealing phenomena. Elsevier, Tarrytown, pp 327–362

[83] Samek L, De Moor E, Penning J, De Cooman BC (2006) Influence of alloying elements on the kinetics of strain-induced martensitic nucleation in low-alloy, multiphase high-strength steels. Metall Mater Trans A Phys Metall Mater Sci 37:109–124. https://doi.org/10.1007/s11661-006-0157-0

[84] Wu W, Hwu LY, Lin DY, Lee JL (2000) Relationship between alloying elements and retained austenite in martensitic stainless steel welds. Scr Mater 42:1071–1076. https://doi.org/10.1016/S1359-6462(00)00339-0

[85] Furuhara T, Kikumoto K, Saito H, Sekine T, Ogawa T, Morito S, Maki T (2008) Phase transformation from fine-grained austenite. ISIJ Int 48:1038–1045. https://doi.org/10.2355/isijinternational.48.1038

[86] Bowles JS, Mackenzie JK (1954) The crystallography of martensite transformations I. Acta Metall 2:129–137. https://doi.org/10.1016/0001-6160(54)90102-9

[87] Mackenzie JK, Bowles JS (1954) The crystallography of martensite transformations II. Acta Metall 2:138–147. https://doi.org/10.1016/0001-6160(54)90103-0

[88] Bowles JS, Mackenzie JK (1954) The crystallography of martensite transformations III. Face-centred cubic to body-centred tetragonal transformations. Acta Metall 2:224–234. https://doi.org/10.1016/0001-6160(54)90163-7

[89] Lieberman DS (1958) Martensitic transformations and determination of the inhomogeneous deformation. Acta Metall 6:680–693

[90] Lieberman DS, Wechsler MS, Read TA (1955) Cubic to orthorhombic diffusionless phase change—experimental and theoretical studies of AuCd. J Appl Phys 26:473–484. https://doi.org/10.1063/1.1722021

[91] Wayman CM (1964) Introduction to the crystallography of martensitic transformations. Introd Crystallogr Martensitic Transform

[92] Wanner T, Fuller ER, Saylor DM (2010) Homology metrics for microstructure response fields in polycrystals. Acta Mater 58:102–110. https://doi.org/10.1016/j.actamat.2009.08.061

[93] Rohrer GS, Miller HM (2010) Topological characteristics of plane sections of polycrystals. Acta Mater 58:3805–3814. https://doi.org/10.1016/j.actamat.2010.03.028